Journal Name

Crossmark

RECEIVED
dd Month yyyy

REVISED
dd Month yyyy

PAPER

Benchmarking DFT functionals for Argon adsorption on Ru(0001): assessment of van der Waals corrections for gas–surface interactions

Carmen A. Tachino[1,2,*] and Cristina Díaz[3]

[1]Grupo de Fisicoquímica en Interfases y Nanoestructuras, Instituto de Física Rosario (CONICET-UNR), Bv. 27 de Febrero 210 bis, S2000 Rosario, Argentina

[2]Facultad de Ciencias Exactas, Ingeniería y Agrimensura, Universidad Nacional de Rosario (UNR), Av. Pellegrini 250, S2000 Rosario, Argentina

[3]Departamento de Química Física, Universidad Complutense de Madrid, 28040 Madrid, Spain

*Author to whom any correspondence should be addressed.

E-mail: tachino@ifir-conicet.gov.ar,crdiaz08@ucm.es

Keywords: density functional theory, van der Waals forces, noble gases, gas-surface interactions

Abstract

Accurately describing the interaction of noble gases with metal surfaces remains a significant challenge for theoretical approaches within density functional theory (DFT). Many methods have been proposed to properly incorporate van der Waals effects into DFT, although none of these approaches has demonstrated sufficient accuracy or transferability for modelling the diffraction of rare gases from surfaces. In this work, we present a systematic benchmark of 18 exchange-correlation functionals within DFT for describing the interaction of Ar with the Ru(0001) surface. Our results show that semi-local functionals consistently underestimate the interaction strength, while those including dispersion corrections tend to overestimate it. These discrepancies have direct implications for modelling gas-surface scattering dynamics. Based on our findings, we conclude that Ar/Ru(0001) can serves as a particularly challenging benchmark system for evaluating dispersion corrections in DFT-based surface science simulations.

1 Introduction

The synergy between experimental studies and theoretical simulations is essential for achieving a comprehensive understanding of the dynamic processes between adsorbates and surfaces [1, 2]. In this context, the interaction of noble gases with metallic surfaces provides a fundamental benchmark for studying a variety of phenomena, such as physisorption processes, surface morphology, surface phonons, and the nature of weak adsorbate–substrate interactions. In particular, diffractive scattering experiments of noble gases at thermal energies (typically below 300 meV) have been widely employed as a non-destructive technique to probe surface properties [3, 4]. From the analysis of diffraction spectra, valuable information can be obtained regarding surface corrugation, adsorption sites, and physisorption potentials.

The theoretical description of the electronic structures of rare gases interacting with metallic surfaces is particularly challenging owing to the influence of van der Waals (vdW) forces, which dominate attractive interactions at large distances [5]. Early attempts to model these systems date back to the early 1980s, when a simple model based on the use of interaction potentials proportional to the unperturbated electronics density of the surface at the position of the atom was proposed [6]. However, this approach soon demonstrated to be too simplistic to accurately describe noble gas-metal surface interactions, as they were more complex than initially appeared [7, 8]. Another simplified description is provided by jellium-based models [9, 10], which can reproduce some general properties of the interaction but fail to account for the corrugation amplitudes, which are responsible for diffraction phenomena. In 2014 a more sophisticated approach was proposed to study the He diffraction from MgO(100), based on a hierarchical combination of second-order Møller-Plesset perturbation theory (MP2) and coupled-cluster calculations (CCSDT(Q)) on surface-model finite cluster [11]. However, this model has not yet been tested in studies of rare-gas

diffraction from metal surfaces. A more natural and computationally efficient framework for these systems is provided by density functional theory (DFT).

Although density functional theory is the most appropriate method for describing periodic or quasi-periodic systems, when rare gases are involved, the use of DFT is limited by its poor description of vdW forces. Nonetheless, DFT simulations within the local density approximation (LDA) [12–16] and the generalized gradient approximation (GGA) [17–19] exchange-correlation functionals have been widely employed to study several rare gas/metal surface systems, yielding dissimilar results [8, 20–24]. Efforts to explicitly include dispersion forces in DFT have led to a variety of promising methods, ranging from those that directly correct Kohn-Sham DFT energies [25–27] to those that correct the exchange-correlation functional by adding a nonlocal electron correlation function [28–31].

However, when applied to rare gas systems, these methods exhibit strong system dependence. For example, Wannier function-based corrections provided more accurate adsorption energies for noble gases interacting with Cu(111) and Pd(111) surfaces compared to standard GGA results [32, 33]. Similarly, the nonlocal optB86-vdW approach [31] reproduces the Ar-Au pair potential in close agreement with the ab initio spin-restricted open-shell coupled cluster calculations (RCCSD(T)) [34], while vdW-DF2 [30] and PBE+D3 [35] tend to overestimate the depth of the potential well. A more comprehensive analysis of the performance of various vdW-DFT approaches in systems involving rare gases has been conducted focusing on the diffraction of Ne and He from Ru(0001) [36, 37]. In the Ne/Ru(0001) case [36], five out of six tested dispersion-corrected functionals (including both empirical and nonlocal vdW approaches) –PBE+D3 [26], vdW-DF [28], vdW-DF2 [30], PBE+vdW^S [27], and PBE+vdW-DF [29]– successfully reproduce the relative intensities of the first-order diffraction peaks, with vdW-DF2 providing the closest quantitative agreement with experiments [38]. In contrast, PBE+D2 [25] failed both qualitatively and quantitatively to reproduce diffraction patterns. Conversely, in the case of He/Ru(0001) [37], none of the tested approaches –whether based on pairwise methods (PBE+vdW^S [27], PBE+MBD [39]) or non-local density functionals (vdW-DF [28], vdW-DF2 [30], vdW-DF-optB86b [29])– were able to accurately reproduce the experimental diffraction patterns, whereas PBE-based calculations showed the closest results to the experimental data.

In this context, it seems important to further explore the capability of proposed approaches to incorporate vdW forces in DFT to describe the diffraction of noble gases by metallic surfaces. Is He diffraction by metal surfaces the only case where current approaches fail even qualitatively? Or, conversely, is Ne diffraction an exceptional case in which these approaches are effective? To address these questions, we propose in this work a systematic study of Ar diffraction from Ru(0001). This system was selected because it allows for direct comparison with the previous He and Ne studies [36, 37], and because experimental data are available at equivalent conditions and using the same setup (see [38]). We present a comprehensive benchmark of 18 different DFT functionals, aimed at evaluating their performance in describing the physisorption potential of Ar on Ru(0001) and identifying potential limitations of dispersion correction methods. It is worth noting that previous works have shown that the non-local approaches vdW-DF [28] and optPBE-vdW [31] best reproduce the adsorption energy of Ar on Au(111) [40], although it is unclear whether these results can be generalized to other Ar/metal systems.

Finally, we examine how variations in the electronic structure of the system, induced by different exchange-correlation functionals, affect the scattering dynamics, emphasizing the critical role that an accurate description of physisorption plays in predicting noble gas diffraction.

2 Computational Methods

To conduct this study, we employed the Born-Oppenheimer Static Surface (BOSS) approximation. In this approach, the electronic structure is first computed with the surface atoms fixed at their equilibrium positions, and the resulting potential energy surfaces are subsequently used to perform the nuclear dynamics.

2.1 DFT calculations

The electronic structure of the Ar/Ru(0001) system was computed using the Vienna Ab-Initio Simulation Package (VASP) code [41–44]. This code uses a plane-wave basis set to obtain the electronic Kohn-Sham orbitals, and the interaction between valence electrons and ionic cores was described using the Projector Augmented-Wave (PAW) method [45, 46]. The plane-wave cutoff energy has been set to 800 eV; this value, obtained from convergence tests, is substantially higher than the typical cutoff energies used in VASP calculations, but it is consistent with those determined in previous calculations involving rare gases [36–38]. The convergence was assessed

using relative energies along the Ar–surface interaction curve, taking as reference the total energy with the Ar atom placed in the middle of the vacuum region. Convergence of the cutoff energy was considered achieved when the variation in relative energy between successive cutoff values was smaller than 0.1 meV for all sampled distances. This seems to indicate that, in general, such systems require high cutoff energies. The Methfessel–Paxton scheme [47] was chosen with a smearing width of 0.2 eV.

The system was modeled as a five-layer Ru(0001) slab plus a 20 Å layer of vacuum, which prevents interactions between periodic images along the surface-normal direction. The coordinate system used throughout this work is shown in figure 1. Each layer of the slab was constructed using a 5×5 surface unit cell with a lattice constant of 2.73 Å [48], ensuring negligible lateral interactions between periodically repeated argon atoms. The first Brillouin zone was sampled with a 3×3×1 Monkhorst-Pack k-point mesh, which was previously tested for convergence.

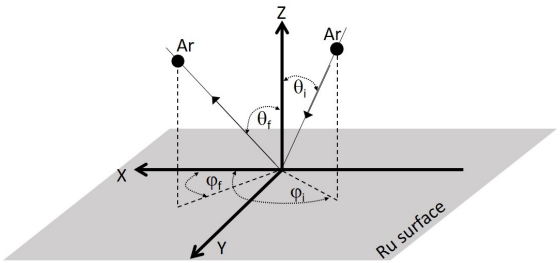

Figure 1: Cartesian (X,Y,Z) coordinate system. The Z direction is perpendicular to the Ru(0001) surface, while the XY plane is parallel to it. The set of polar and azimuthal angles (θ_i, φ_i) indicates the argon incidence direction. Analogously, (θ_f, φ_f) represents the reflection one.

2.2 Exchange-correlation functionals

The choice of exchange-correlation (XC) functionals in this study was guided by previous works on the diffraction of noble gases such as neon and helium from Ru(0001) surfaces, where several strategies to incorporate van der Waals interactions were tested with varying degrees of success [36, 37]. Here, we extend that approach by systematically comparing a broad set of 18 functionals across seven different families, in order to assess their ability to describe the Ar/Ru(0001) interaction at both short and long ranges.

The selected functionals can be grouped as follows:

- GGA (semi-local): PW91, PBE, revPBE, rPBE, and PBEsol, which neglect long-range dispersion interactions.
- GGA with empirical dispersion corrections: PBE+D2, PBE+D3, and Tkatchenko–Scheffler (TS), which include pairwise atomic dispersion terms added to standard GGA energies.
- vdW-DF family: vdW-DF, vdW-DF2, vdW-DF-cx, and rev-vdW-DF2, which incorporate nonlocal correlation functionals to capture dispersion forces self-consistently.
- vdW-optimized GGAs: optB86b-vdW, optB88-vdW, and optPBE-vdW, which employ exchange functionals optimized for use with nonlocal correlation terms to improve binding energies.
- GGA with non-local correlation: rVV10, which combines the standard semi-local PBE with the rVV10 nonlocal correlation functional.
- Meta-GGA with nonlocal dispersion: SCAN+rVV10, which couples the SCAN meta-GGA with the rVV10 nonlocal correlation functional, providing an improved description of both short- and long-range interactions.
- vdW-DF3 family: vdW-DF3-opt1 and vdW-DF3-opt2, representing the most recent generation of nonlocal functionals, designed to improve long-range correlation with parameters optimized for gas-surface systems.

This comprehensive selection enables a consistent comparison of how empirical and nonlocal dispersion corrections influence the predicted potential energy surfaces (PESs) of Ar on Ru(0001). For clarity and ease of reference, table 1 summarizes all the XC functionals employed in this work, including their treatment of dispersion interactions and the corresponding references.

Table 1: Exchange–correlation functionals employed in this study, classified according to their treatment of dispersion interactions. The corresponding family or category and bibliographic references are also indicated.

#	**Functional**	**Dispersion Treatment**	**Family/Category**	**Ref.**
1	PW91	None	GGA (semi-local)	[18]
2	PBE	None	GGA (semi-local)	[19]
3	revPBE	None	GGA (semi-local)	[49]
4	rPBE	None	GGA (semi-local)	[50]
5	PBEsol	None	GGA (semi-local)	[51]
6	PBE+D2	Empirical (pairwise, D2)	GGA+empirical dispersion	[25]
7	PBE+D3	Empirical (pairwise, D3)	GGA+empirical dispersion	[26]
8	TS	Empirical (Tkatchenko-Scheffler)	GGA+empirical dispersion	[52]
9	vdW-DF2	Non-local correlation (self-consistent)	vdW-DF family	[30]
10	vdW-DF-cx	Non-local correlation (self-consistent)	vdW-DF family	[53]
11	rev-vdW-DF2	Non-local correlation (revised)	vdW-DF family	[54]
12	optB86b-vdW	Non-local correlation	vdW optimized GGA	[29]
13	optB88-vdW	Non-local correlation	vdW optimized GGA	[31]
14	optPBE-vdW	Non-local correlation	vdW optimized GGA	[31]
15	rVV10	Non-local correlation	GGA+non-local correlation	[55]
16	SCAN+rVV10	Non-local correction (Meta-GGA base)	Meta GGA+rVV10	[56]
17	vdW-DF3-opt1	Non-local correlation (DF3-optimized)	vdW-DF3 family	[57]
18	vdW-DF3-opt2	Non-local correlation (DF3-optimized)	vdW-DF3 family	[57]

2.3 Adsorption sites and sampling

To study Ar adsorption on Ru(0001), seven high-symmetry adsorption sites within the irreducible surface unit cell were selected, as shown in figure 2(a). It should be noted that Ru(0001) has a hexagonal $C_{3\nu}$ symmetry; however, the hollow-fcc and hollow-hcp sites are nearly degenerate in energy, allowing the use of an effective $C_{6\nu}$ symmetry instead of the exact C_{3v} one [48]. This approximation minimizes the size of the irreducible unit cell and thus reduces the number of requiered DFT calculations and the overall computational cost.

Since we aimed to obtain the full one-dimensional (1D) potential well, in addition to the adsorption energy, the total energy was evaluated for each site with the Ar atom fixed at various vertical distances (z) above the ruthenium surface. The z values ranged from -0.75 Å to 7.75 Å for semi-local functionals and up to 9.75 Å for functionals including dispersion corrections, with $z = 0$ Å defined as the position of the outermost Ru plane. The sampling range was chosen to encompass the physically relevant region of the physisorption potential well and the asymptotic regime.

2.4 3D Potential energy surface

After analyzing the adsorption sites and based on the obtained results, we selected a subset of representative functionals (see Section 3) to compute five full three-dimensional (3D) potential energy surfaces (PESs). To built these PESs, we applied the well-stablished Corrugation Reducing Procedure (CRP) [58] to the sets of DFT data obtained for the adsorption sites. This method minimizes numerical instabilities associated with direct interpolation by decomposing the total 3D potential energy surface (V_{3D}) as follows:

$$V_{3D}(\mathbf{R}) = I_{3D} + \sum_i V_{1D}(\mathbf{r}_i), \tag{1}$$

where $V_{1D}(\mathbf{r}_i)$ is a corrugated function representing the one-dimensional potential between the atomic projectile and the i-th surface atom, separated by distance $\mathbf{r}_i$. I_{3D} is a smoother function, interpolated along the Z-axis using cubic splines and in the (X,Y) plane using a symmetry-adapted Fourier expansion. This procedure has been extensively used to construct full PESs for atom/surface systems, including metallic [36, 37, 59, 60] and insulating surfaces [61–65].

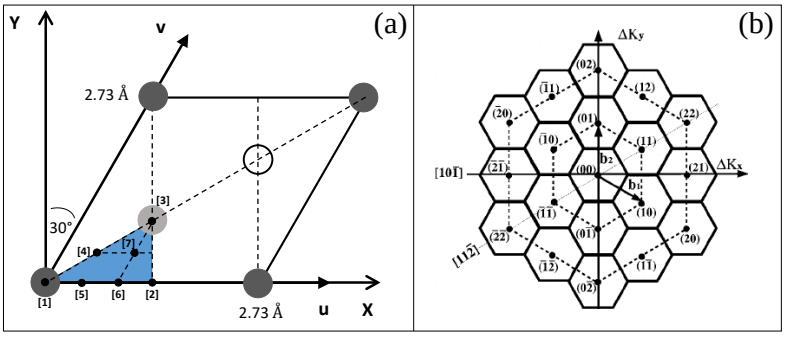

Figure 2: (a) Schematic representation of the Ru(0001) cell used in electronic structure calculations. Dark gray circles: topmost layer Ru atoms. Light gray circles: second-layer Ru atoms. The white circle does not represent an argon atom, but a hollow-fcc site. The shaded area shows the irreducible unit cell over which calculations were performed, with the black dots indicating the symmetry sites: [1] top, [2] bridge, [3] hollow-hcp, [4] midway between top and hollow-hcp, [5] third of the way between top and bridge, [6] third of the way between bridge and top, [7] midway between site [6] and hollow-hcp. Cartesian (XY) and crystalline (uv) axes are also shown for clarity. (b) Reciprocal lattice for Ru(0001): hexagons represent the Wigner-Seitz cells, while numbers withing parentheses indicate the related diffraction peaks.

The accuracy of the interpolation was evaluated by comparing the interpolated PES energies with a subset of DFT reference data not included in the fitting process. The resulting average deviations were found to be smaller than 5×10^{-4} eV, confirming that the electronic structure of the molecule and surface depends on the precision of the underlying energy data set employed in the interpolation.

2.5 Dynamics

The scattering of Ar atoms from Ru(0001) was studied using classical trajectory simulations, by numerically solving Hamilton's equations of motion with the predictor-corrector algorithm proposed by Burlisch and Stoer [66]. Scattering probabilities were computed as a function of the final polar and azimuthal angles, θ_f and φ_f (see figure 1 for definitions)

For each incident energy E_i and incidence direction (θ_i,φ_i), a microcanonical ensemble of 200,000 initial conditions (X_i, Y_i) was used to ensure low statistical errors. In all trajectories, the initial coordinate of the projectile normal to the surface was set to $Z_i = 9.70$ Å in the case of vdW-corrected functionals and to $Z_i = 7.70$ Å in the case of GGAs, and the integration was continued until the final coordinate Z_f exceeded Z_i, or until reaching a maximum integration time of 15 ps. If the latter condition was met, the atom was considered dynamically trapped on the surface.

The scattering probabilities were obtained as:

$$P(\theta_f, \varphi_f) = \frac{N(\theta_f, \varphi_f)}{N_T} \tag{2}$$

and

$$P(\theta_f) = \frac{\sum_{\varphi_f=0}^{\varphi_f=2\pi} N(\theta_f, \varphi_f)}{N_T}, \tag{3}$$

where N_T represents the total number of integrated trajectories, and $N(\theta_f, \varphi_f)$ the number of trajectories scattered with final angles θ_f and φ_f.

In classical mechanics, the effects of quantization are usually incorporated by discretizing the continuous distribution, where all values within a certain interval are associated with a single quantum value. Building on this concept, Ray and Bowman proposed in 1975 a discretization method that makes classical calculations compatible with Bragg's diffraction law [67–69]. Following the proposed method, the probability of a specific (n,m) diffraction transition is determined as the fraction of trajectories whose parallel momentum change lies within the two-dimensional Wigner-Seitz cell centered around the (n,m) lattice point in reciprocal space (see figure 2(b)).

This discretization method has been shown to yield relative diffraction intensities that agree well with both quantum calculations and experimental measurements for various projectile-surface systems, including atomic [61] and molecular [70–75] projectiles.

The combined use of high-accuracy PESs and large-scale classical trajectory simulations provides a robust framework for analyzing the influence of exchange–correlation functionals on the dynamics of Ar from Ru(0001).

In addition, to complement the classical dynamics results and provide a quantum perspective on the scattering process, we have performed quantum dynamics simulations using the Heidelberg implementation [76] of the Multiconfiguration Time-Dependent Hartree (MCTDH) method [77–80]. These calculations were carried out using the PBE potential energy surface as a representative case due to its well-characterized shape and moderate computational cost. Here, only a brief description of the MCTDH method is provided, as the theoretical details have been extensively discussed elsewhere (see, for instance, Ref. [78]). Within MCTDH, the time-dependent nuclear wave function is expressed as a linear combination of products of time-dependent single-particle functions (SPFs), whose evolution is obtained variationally through the Dirac–Frenkel principle. This formulation allows an efficient propagation of multidimensional quantum wave packets and has been successfully applied to atomic and molecular scattering and diffraction from both metallic and ionic surfaces [36,37,63,81–91]. The potential energy surface was represented in a separable product form using the POTFIT algorithm [92,93], and the dynamics were propagated for incidence conditions matching the experimental ones and the classical simulations ($E_i = 26$ meV, $\theta_i = 45°$, $\varphi_i = 30°$). The MCTDH simulations thus provide a quantum-mechanical counterpart to the classical trajectory calculations, allowing a direct comparison of scattering observables and diffraction probabilities on the same potential energy surface.

3 Results and Discussion

3.1 Analysis of the PES

In figures 3(a)-3(e), we present the one-dimensional potential energy curves for Ar/Ru(0001) as a function of the atom-surface distance, z, at the top site for 18 different XC functionals. For clarity, the simulations have been grouped into five categories: (a) pure GGA functionals [18,19,49–51]; (b) empirical pairwise corrections [25,26,52]; (c) the vdW-DF family [30,53,54]; (d) vdW-optimized GGA functionals [29,31]; and (e) the meta-GGA+vdW and vdW-DF3 family [55–57]. The figure also includes the results by Minniti et al. [38], who fitted experimental data using the three-parameter Morse potential:

$$V(z) = D_0 \left[\exp\left(-2\,\alpha\,(z - z_0)\right) - 2\,\exp\left(-\alpha\,(z - z_0)\right)\right]. \tag{4}$$

where the experimental parameters are $D_0^{(exp)}$=65 meV (well depth), $\alpha^{(exp)}$=1.395 Å^{-1} (range), and $z_0^{(exp)}$=3.50 Å (equilibrium distance). As explained in Ref. [38], these values were obtained using a variational fitting procedure applied to the measured diffraction intensities, in which $z_0^{(exp)}$ was kept constant, while $D_0^{(exp)}$ and $\alpha^{(exp)}$ were optimized.

Figure 3(a) shows the 1D energy curves obtained with five GGA functionals. The potential wells predicted by the GGAs are significantly shallower and generally located at larger distances from the surface than the experimental reference. Among them, PBEsol provides the best agreement with experimental results: it accurately reproduces the equilibrium position around 3.5 Å, and although the well depth is largely underestimated, it (together with PW91) yields the closest values to the experimental data. Conversely, the poorest performance is observed for revPBE, which largely overestimates the equilibrium distance and underestimate the well depth, resulting in a nearly flat energy profile.

A more direct comparison with the experimental data can be made by fitting the DFT results to the Morse potential of equation 4, allowing D_0, z_0, and α to vary freely. The fitted parameters are summarized in table 2. These results clearly demonstrate that semi-local GGAs fail to reproduce the main characteristics of the experimental physisorption well, as none of the fitted parameters match those reported by Minniti *et al.* [38]. This findings is consistent with previous results for Ne/Ru(0001) [36], where GGA functionals systematically underestimated the experimental well depth.

To evaluate the influence of dispersion corrections, figures 3(b)-3(e) and table 2 present the one-dimensional energy curves obtained for the four families of van der Waals (vdW) approaches mentioned above. In general, all vdW methods improve upon the best GGA results. A detailed inspection shows that pairwise-corrected functionals presented in figure 3(b), predict equilibrium distances in closest agreement with the experimental value; in fact, PBE+D3 and TS match it

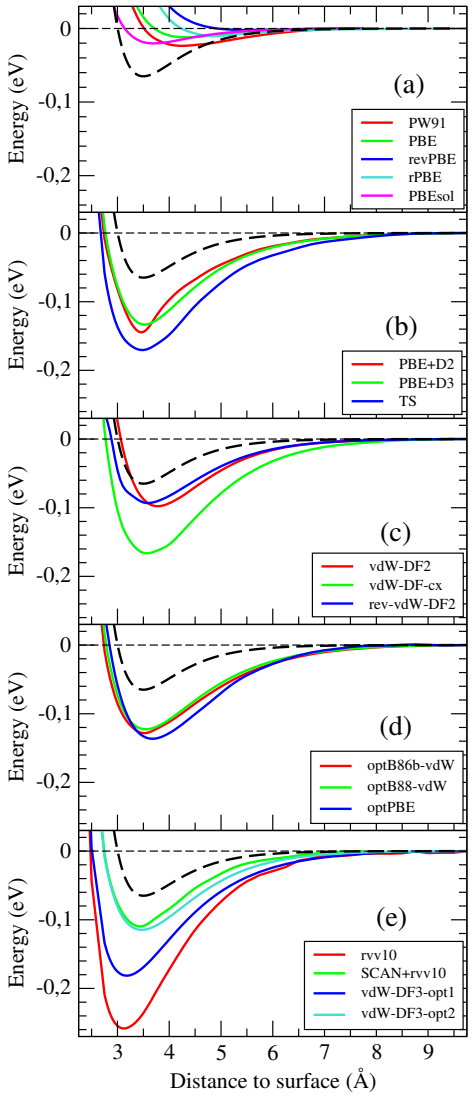

Figure 3: Potential energy curves for Ar approaching the Ru(0001) surface along the top site, obtained with the exchange-correlation functionals listed in table 1. The panels group the functionals by dispersion treatment: (a) semi-local GGA, (b) empirical pairwise corrections, (c) vdW-DF family, (d) vdW-optimized GGA, and (e) meta-GGA + vdW and vdW-DF3 family. The dashed black curves in each panel represent a Morse-type potential fitted to experimental estimates [38].

almost exactly. However, all three pairwise-corrected functionals significantly overestimate the well depth, by more than a factor of two. In contrast, in figure 3(c) it can be seen that the vdW-DF family yields the best agreement for the well depth. In particular, vdW-DF2 and rev-vdW-DF2 overestimates D_0 by less than 50%, and slightly overestimate the equilibrium distance, with values of 3.80 Å and 3.60 Å respectively. The vdW-optimized GGA functionals in figure 3(d) display very similar behaviour among themselves: they overestimate the well depth by about a factor of two but reproduce z_0 reasonably well, except for optPBE-vdW, which slightly overestimates it.

Finally, the meta-GGA+vdW and vdW-DF3 families in figure 3(e) show the most dissimilar results within the group. Although all of these functionals overestimate the well depth, they differ from the other families by predicting smaller equilibrium distances than the experimental reference. Within this set, SCAN-rVV10 provides the closest agreement with experimental data. Indeed, among all 18 functionals analyzed, SCAN+rVV10 provides the most accurate potential well when compared to the experimental data.

3.2 Energetic and Geometric Corrugation

To further analyze how the electronic structure depends on the DFT functional used, we present in figure 4(a) the adsorption energy for seven sites within the Ru(0001) irreducible unit cell (see figure 2 and the inset of figure 4(b)), which provides insight into the energetic corrugation. Figure 4(b)

Table 2: Parameters describing the potential well for GGA and vdW-corrected functionals. Values for depth (D_0), equilibrium position (z_0), and range (α) were obtained by fitting the DFT data to the Morse potential of equation (4).

Functional	$\mathbf{D_0}$ **(meV)**	$\mathbf{z_0}$**(Å)**	α**(Å^{-1})**
PW91	23.60	4.25	0.933
PBE	12.00	4.35	1.159
revPBE	2.02	5.50	1.144
rPBE	10.53	4.85	1.092
PBEsol	20.29	3.70	1.266
PBE+D2	144.64	3.45	1.009
PBE+D3	133.30	3.50	0.963
TS	170.40	3.50	0.916
vdW-DF-cx	166.38	3.55	0.899
vdW-DF2	97.80	3.80	0.993
rev-vdW-DF2	93.36	3.60	0.880
optB86b-vdW	128.27	3.50	0.902
optB88-vdW	122.61	3.55	0.944
optPBE-vdW	136.35	3.70	0.889
rVV10	260.00	3.13	1.015
SCAN+rVV10	112.70	3.45	1.097
vdW-DF3-opt1	181.40	3.20	0.980
vdW-DF3-opt2	120.00	3.43	0.999
Morse [38]	65.00	3.50	1.395

shows z_0 –the vertical distance at which the potential well minimum occurs– offering an indication of the geometric corrugation. In this analysis, we considered nine representative DFT functionals from the different families listed in table 1. These were selected to cover the full spectrum of GGAs (PBE, PW91, and PBEsol) and dispersion-correction schemes, ranging from semi-empirical to fully nonlocal and meta-GGA formulations (PBE+D3, optB86b-vdW, vdW-DF2, rev-vdW-DF2, rVV10, and SCAN+rVV10). This selection allows a systematic assessment of how van der Waals interactions influence both the depth and the corrugation of the physisorption potential.

Figure 4(a) clearly shows once again that dispersion-corrected functionals (PBE+D3, optB86b-vdW, vdW-DF2, rev-vdW-DF2, rVV10, and SCAN+rVV10) predict deeper potential wells than the semi-local GGAs (PBE, PW91, and PBEsol). Among these, PBE produces the shallowest well, while rVV10 yields the deepest. It can also be observed that the amplitude of the corrugation –defined as the energy difference between the most and least favorable adsorption sites– slightly increases when dispersion interactions are included. Among the dispersion-corrected functionals, rVV10 exhibits the largest energetic corrugation, whereas vdW-DF2 shows the smallest. In contrast, the GGA functionals display very smooth lateral variations, consistent with a weakly corrugated energy landscape.

The geometric corrugation in figure 4(b) exhibits similar lateral trends for most functionals, with two notable exceptions. For PW91, z_0 decreases slightly from site [1] (top) to [5], then increases almost linearly along the [5]–[6]–[2]–[7]–[3] path direction, and reaches its maximum at site [3] (hollow) before decreasing again at site [4]. This behaviour indicates a distinctly anisotropic geometric corrugation, with the highest adsorption height located at the hollow site. In contrast, PBE+D3 produces an almost flat curve with minimal variation between sites, reflecting a significantly reduced geometric corrugation. As shown in figure 4(a), the rVV10 functional stands out from the other vdW functionals by predicting the smallest z_0 values, placing Ar closest to the surface. Meanwhile, the PBEsol GGA functional yields z_0 values comparable to those of the vow-corrected functionals, setting it apart from other GGAs such as PBE and PW91.

Overall, these results highlight that, while dispersion primarily impacts the depth of the potential wells, the overall corrugation pattern imposed by the Ru(0001) surface remains largely consistent across all functionals. However, even small variations in both energetic and geometric corrugation are likely to influence the scattering dynamics, affecting the balance between specular and diffuse reflection channels.

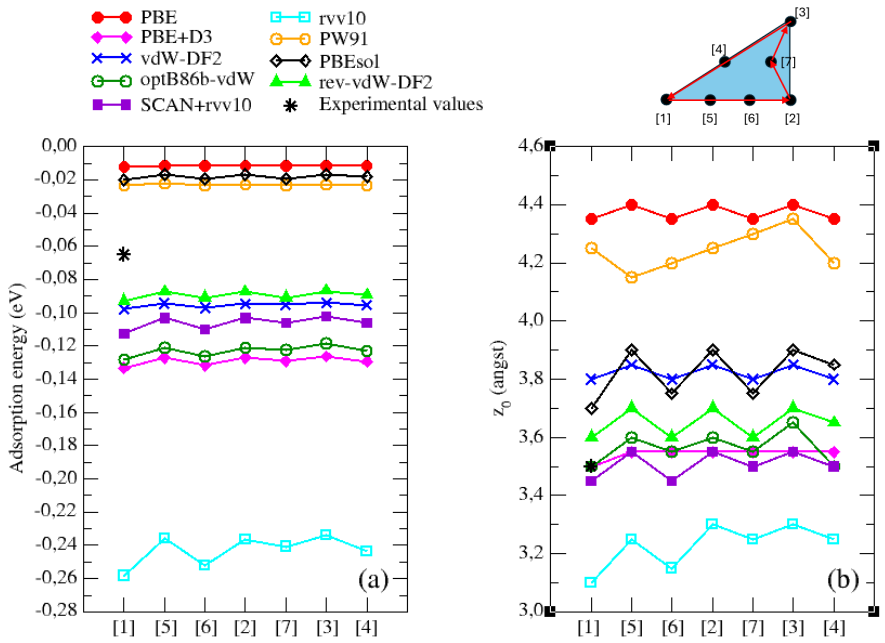

Figure 4: Energetic (a) and geometric (b) corrugation of the Ar/Ru(0001) system obtained with nine representative DFT functionals, for the seven symmetry-cell sites shown in figure 2(a). The energetic corrugation corresponds to the adsorption energy at the potential minimum for each high-symmetry site, while the geometric corrugation represents the corresponding equilibrium height z_0. The sites are ordered along the abscissa according to the sequence indicated by the red arrows in the schematic figure of the irreducible unit cell. Experimental reference values [38] are also included.

3.3 Impact of PES accuracy on classical scattering dynamics

To assess the influence of van der Waals (vdW) corrections on the scattering dynamics of Ar on Ru(0001), we have performed classical trajectories simulations for five representative functionals: PBE, vdV-DF2, PBE+D3, optB86b-vdW, and SCAN+rVV10. The first two functionals were selected because they yielded the best results for the scattering of He [37] and Ne [36] from Ru(0001), respectively. PBE+D3 was chosen as it is the member of the pairwise-correction family that most closely reproduces the experimental adsorption characteristics (see figure 3(b)). The optB86b-vdW functional represents the most accurate among vdW-optimized GGA family functionals, while SCAN+rVV10 provides the best overall description of the physisorption potential.

Following the experimental conditions reported by Minitti *et al.* [38], the incidence direction was fixed along the $[11\bar{2}]$ crystallographic direction. In all simulations, trajectories were propagated on rigid potential energy surfaces (PESs), allowing us to isolate the effects of PES morphology and vdW corrections on the dynamics. It should be noted that this approximation neglects energy transfer to phonons. Although previous experimental and theoretical studies have shown that substrate vibrations can contribute to dissipation and enhance transient trapping [94–97], they are not expected to significantly modify the scattering or diffraction distributions [74]. Two sets of initial conditions were considered: (i) E_i=26 meV with $\theta_i = 45°$, and (ii) E_i=64 meV with $\theta_i = 35°$.

Based on the analysis of the scattering channels at the end of each trajectory integration, two distinct mechanisms have been identified: (i) direct scattering, where the atom escapes back into the vacuum after a single rebound, and (ii) trapping-mediated scattering, where the atom remains temporarily trapped, undergoing two or more rebounds before desorbing. This analysis revealed that at 26 meV, trapping occurred only for vdW-corrected functionals, consistent with their deeper and more attractive potential wells. In contrast, the standard GGA functional (PBE) exhibited only direct scattering. At 64 meV, evidence of transient trapping has only been observed for optB86b-vdW and SCAN+rVV10.

We first analyze the angular distributions obtained from classical trajectory simulations. This provides a direct insight into how the surface morphology and the depth of the interaction potential influence the scattering process, complementing the information derived from the adsorption energetics.

To capture the full correlation between the final polar (θ_f) and azimuthal (φ_f) angles, figure 5

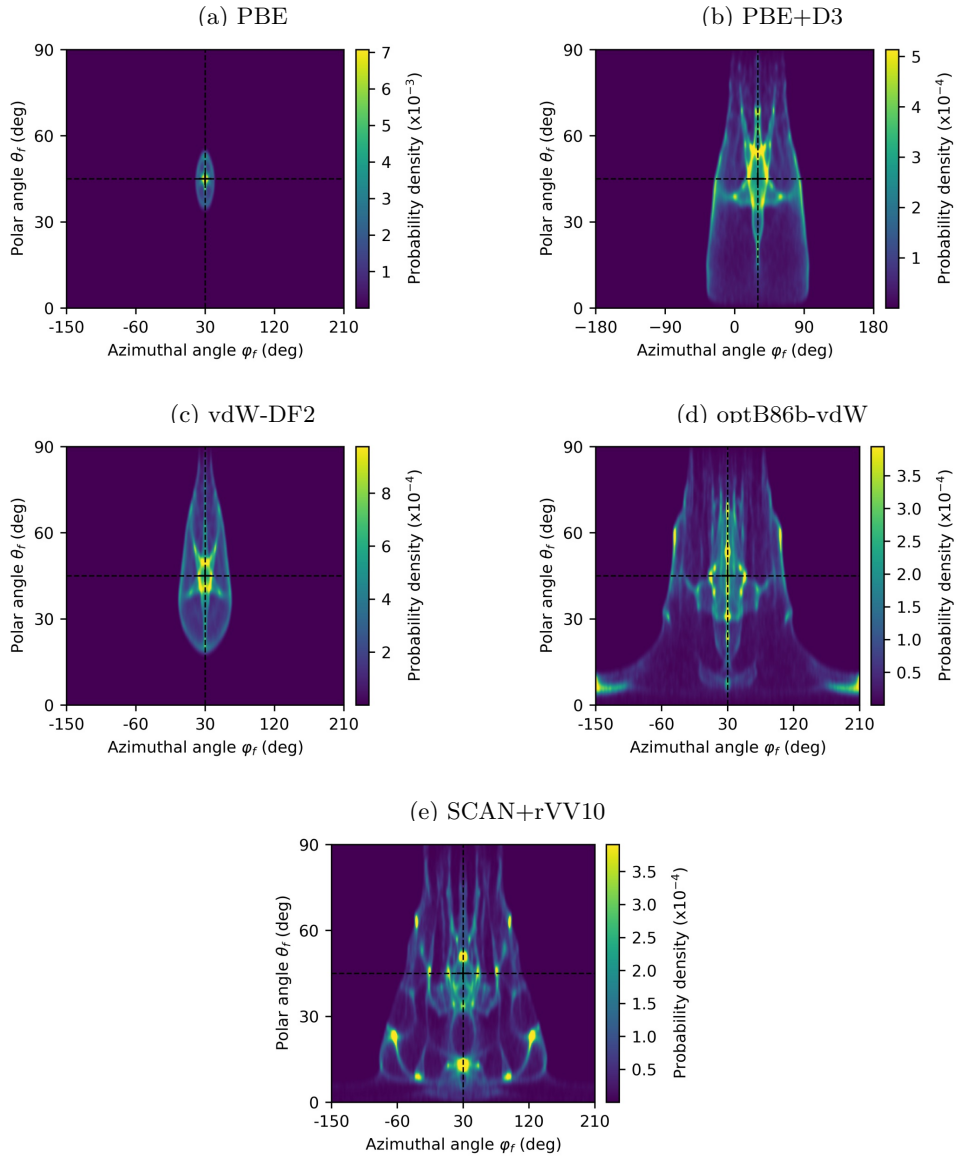

Figure 5: 2D angular distributions for final reflection direction given by (θ_f, φ_f), for single-bounce trajectories at E_i =26 meV, φ_i=30° and θ_i = 45°: a) PBE. b) PBE+D3. c) vdW-DF2. d) optB86b-vdW. e) SCAN+rVV10.

presents two-dimensional heatmaps of the scattered trajectories. These visualizations offer an intuitive view of how potential corrugation influences the reflection pattern at E_i=26 meV, $\varphi_i = 30°$, and $\theta_i = 45°$. Each panel corresponds to one of the selected functionals: a) PBE, b) PBE+D3, c) vdW-DF2, d) optB86b-vdW, and e) SCAN+rVV10.

For PBE, the distribution in figure 5(a) is narrowly localized around the specular direction ($\theta_f = \theta_i$, $\varphi_f = \varphi_i$), with negligible intensity elsewhere, indicating predominantly elastic, quasi-specular reflection. This behaviour aligns with the shallow corrugation and weak physisorption well predicted by PBE (see figure 3(a) and table 2), which results in limited lateral steering and a low probability of off-specular scattering.

In the case of PBE+D3, the heatmap in figure 5(b) shows a main lobe centered near the specular direction but with a broader and more diffuse distribution. This behaviour stems from the deeper potential well introduced by the D3 dispersion correction, which increases the residence time of the Ar atom near the surface and enhances transient trapping. Consequently, trajectories undergo stronger energy exchanges and lose some directional correlation, resulting in a more isotropic broadening of the reflected flux.

For vdW-DF2, the reflected intensity remains concentrated around the specular direction,

consistent with the nearly flat energetic and geometric corrugation profiles shown in figures 4(a)-4(b). The weak lateral modulation of the potential suppresses significant steering and lateral deflections, leading to primarily quasi-specular reflection. Nonetheless, a slight azimuthal broadening of the main intensity spot is observed. Overall, the smooth potential landscape predicted by vdW-DF2 results in predominantly elastic and directionally coherent scattering.

The angular distribution for optB86b-vdW in figure 5(d) displays a wider intensity profile, indicating increased lateral deflection and a higher degree of diffuse scattering. This aligns with the more pronounced energetic and geometric corrugation observed for this functional, as shown in figures 4(a)-4(b). Although its average adsorption well depth is comparable to that of PBE+D3, the lateral variations are more significant, producing steeper energy gradients across the surface. The resulting potential landscape favors off-specular scattering and diminishes the directional coherence of the reflected flux, consistent with the more corrugated character of the optB86b-vdW surface.

Finally, for SCAN+rVV10, the heatmap in figure 5(e) displays the broadest and most irregular angular distribution among the five functionals analyzed. Multiple overlapping lobes surround the specular direction, indicating a coexistence of direct and trapping-mediated scattering events. The reflected intensity spreads widely in both θ_f and φ_f angles, indicating a substantial loss of directional coherence and an increase in diffuse scattering. This behaviour results from the combination of a deep and highly corrugated potential energy surface, which promotes transient trapping and multiple rebounds prior desorption.

3.4 Diffraction

To compare our classical scattering results with experimental data, we have simulated diffraction probabilities using the binning method described in subsection 2.5. In figure 6, we present the simulated diffraction probabilities for first- (left panel) and second-order peaks (right panel), alongside the experimental results from Ref. [38], obtained for an incidence energy of 26 meV. In all cases, the theoretical probabilities were normalized to the intensity of the specular peak obtained with the same PES, following the procedure used in previous studies of rare-gas scattering from Ru(0001) [36,37]. This normalization allows for a consistent comparison between the simulated probabilities and the experimental peaks, which are also reported relative to the specular peak [38]. Additionally, during the binning process, we only considered direct scattering events, since trajectories involving multiple rebounds quickly lose the phase coherence necessary for diffraction and therefore only contribute to the incoherent background, which is typically subtracted in experimental analyzes.

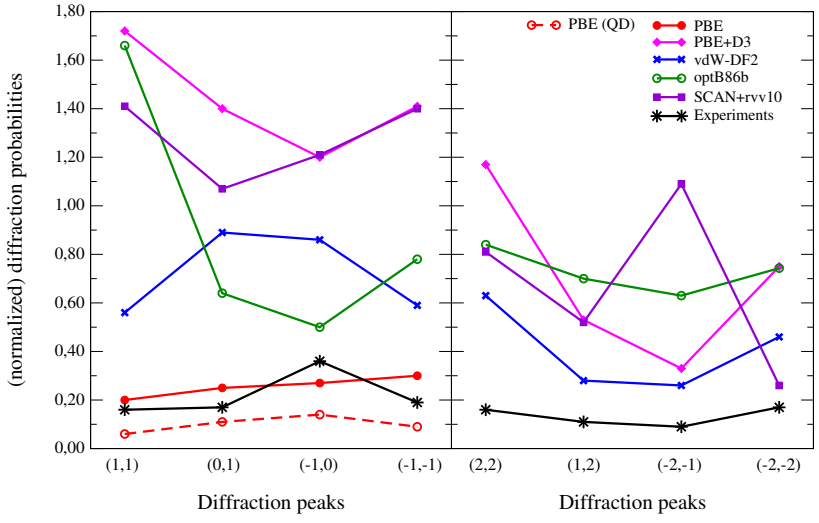

Figure 6: Diffraction probabilities, normalized to the specular peak intensity, for argon impinging with E_i =26 meV, $\varphi_i = 30°$ and $\theta_i = 45°$. Left panel: first order peaks. Right panel: second order peaks. Solid (dashed) lines correspond to probabilities calculated with classical (quantum) models.

From figure 6, it is evident that all vdW functionals overestimate the experimental intensities for both first- and second-order diffraction peaks. Moreover, none of the vdW functionals can even qualitatively reproduce the experimental trends. Interestingly, PBE+D3 and SCAN+rVV10 produce the highest first-order diffraction probabilities, while optB86b-vdW yields the highest second-order diffraction probabilities. Conversely, vdW-DF2 provides the diffraction probabilities

that are closest to the experimental values. However, even in this case, the probabilities are up to a factor of 4 higher than the measured first-order peaks and up to a factor of 2.5 higher than the measured second-order peaks. Additionally, figure 6 shows that the semi-local PBE-GGA functional provides the best overall agreement with the experimental first-order peaks, although it does not predict any second-order diffraction, that according to experimental finding should be similar in intensity to the first-orders ones.

To complement the classical scattering analysis and assess quantum effects, we have also performed quantum dynamics simulations using the Multiconfiguration Time-Dependent Hartree (MCTDH) method on the PBE potential energy surface. This functional was chosen because it represents the least corrugated case and exhibits no trapping within the classical regime, making it a suitable reference for isolating purely quantum diffraction effects while keeping the computational cost within feasible limits. More corrugated or deeper PESs usually require a considerably larger number of POTFIT and MCTDH parameters to achieve convergence leading to an exponential increase in computational cost. These simulations were carried out under the same initial conditions as those used for classical trajectory integration. Prior to propagation, the initial wave function of the argon atom in the non-interaction region (at a sufficiently large distance from the surface) was defined as a product of a Gaussian wave packet for the normal coordinate and plane waves for the parallel translational motion. Both the parameters used in the present MCTDH calculations, and the relevant POTFIT parameters for the PBE potential energy surface are summarized in table 3.

Table 3: Numerical parameters used in MCTDH and POTFIT calculations, and in the definition of the Complex Absorbing Potential (CAP). FFT denotes Fast Fourier Transform. The symbols u and v represent the crystal coordinates defined in figure 1. The CAP parameters b, z_c, and η correspond to the polynomial order, the starting position, and the strength of the CAP, respectively. Δrms and $max(\epsilon)$ represent the root-mean-square and the maximum errors, respectively.

MCTDH		POTFIT	
Initial Wave Packet		*Natural Potentials basis*	
Width, Δz_0 (Å)	0.9	N_x, N_y, N_z	50, 50, contr
Position, z_0 (Å)	9.5		
Primitive Grid		*Relevant fit region*	
Type u, v, z	FFT	z (Å)	> 0
u, v–range (Å)	0.00–10.92	V (eV)	< 3
N_u, N_v	720	V_{cut} (eV)	5
z–range (Å)	-0.75–15.00		
N_z	324		
Wave Packet		*Accuracy*	
SPF u, v, z	12, 12, 12	N_{iter}	6
Propagation Time (fs)	6000–8000	Δrms (meV)	
		Relevant region	0.008–0.011
Complex Absorbing Potential		All grid points	0.28–0.44
b	2	$max(\epsilon)$ (meV)	
z_c (Å)	8.50	Relevant region	1.02–1.12
η (a.u.)	3.15×10^{-6}	All grid points	31.1–85.6

First-order diffraction probabilities for E_i=26 meV and $\theta_i = 45°$ are presented in the left panel of figure 6. As in the classical simulations, the quantum results have been normalized to the corresponding specular peak intensity. From the analysis of figure 6, we observe that quantum probabilities follow the same trend as classical probabilities, although quantum intensities are consistently lower. This overestimation of diffraction probabilities at the classical level, has been consistently reported in systems previously studied with this approach [70,75]. A more quantitative agreement between classical and quantum dynamics could be obtained by weighting the classical trajectories using a Gaussian binning, as proposed in Refs. [98,99]. From this figure, we also observe that quantum first-order diffraction peaks are lower than the experimental ones.

In addition to the results at 26 meV discussed above, we have performed similar calculations at a incident energy of 64 meV. Although these simulations are not shown here, they confirm the same qualitative trends: dispersion-corrected functionals systematically overestimate the diffraction intensities, with vdW-DF2 providing the best overall agreement, while GGA functionals tend to

underestimate the experimental values.

4 Conclusions

In this work, we presented a systematic benchmark study of 18 exchange-correlation functionals within Density Functional Theory to describe the interaction of Ar with Ru(0001). To accomplish this goal, we have calculated the electronic structure of the system partially, only at the top adsorption site, for all functionals, and fully, a continuous potential energy surface (PES) for five selected functionals: PBE, PBE+D3, vdW-DF2, optB86b-vdW and SCAN+rvv10. For these latter functionals, we also performed dynamics simulations.

Our analysis reveals that none of the tested functionals provides a fully satisfactory quantitative description of the experimental physisorption well at the top site. While some functionals reproduce the equilibrium distance reasonably well, significant discrepancies remain in the attractive region, highlighting the difficulty of accurately modelling Ar/Ru(0001) interactions even when dispersion corrections (empirical or nonlocal) are included. These discrepancies directly affect the gas-surface scattering dynamics, especially in the prediction of diffraction probabilities, where sensitivity to the repulsive barrier and the potential well is critical. Our results indicate that the Ar/Ru(0001) system could serve as a rigorous benchmark for evaluating vdW methods, exposing the limitations of the interaction description, particularly in the repulsive region.

These findings contrast with those of del Cueto *et al.* for Ne/Ru(0001) [36], where vdW+DF2 was identified as the functional capable of reproducing diffraction peaks with some accuracy. In fact, our results are somewhat aligned with previous studies on He/Ru(0001) [37], which showed that PBE-based results tend to agree more closely with experimental data than vdW functionals.

In summary, Ar/Ru(0001) emerges as a stringent benchmark for evaluating dispersion correction schemes in surface science. Our results highlight the need for more accurate and transferable approaches to modelling non-local correlation effects. In this context, the random phase approximation (RPA), which has shown good performance in describing CO adsorption [100] and the dissociative chemisorption barriers of H_2 [101] on metal surfaces, could be a promising alternative to explore.

Data availability

The data that support the findings of this study are available from the corresponding author upon reasonable request.

Acknowledgments

C.A.T. acknowledges financial support from the ANPCyT Project No. PICT-2021-I-A-01135, CONICET Project No. PIP 1679, and UNR Project No. PID 80020190100011UR (Argentina). C.D. acknowledges support from the Spanish Ministry of Science and Innovation through grant No. PID2022-138288NB-C33. Authors acknowledge the computer time provided by CCT-Rosario Computational Center, member of the High Performance Computing National System of Argentina (SNCAD), and the CCC-UAM for allocation of computer time. C.A.T. acknowledges the warm hospitality of all members of the Department of Chemistry (Module 13) at the Universidad Autónoma de Madrid during her one-year stay. She is particularly grateful to Marcos del Cueto for his assistance and valuable discussions regarding the computational resources and methods used in this study, and to Fernando Martín for the fruitful discussions.

Author contributions

C.A.T performed all the DFT calculations as well as the classical and quantum simulations, and wrote the first draft of the manuscript. She also participated in the preparation and revision of the final version. C.D. supervised the research during C.A.T.'s stay at the Universidad Autónoma de Madrid and contributed to the writing and revision of the manuscript.

Conflict of interest

The authors have no conflicts to disclose.

Ethical statement

This work is purely theoretical and computational. No experiments involving humans or animals were conducted. The authors declare that there are no ethical issues associated with the research presented in this manuscript.

References

[1] Jardine A P, Dworski S, Fouquet P, Alexandrowicz G, Riley D J, Lee G Y H, Ellis J and Allison W 2004 *Science* **304** 1790–1793

[2] Alexandrowicz G, Jardine A P, Fouquet P, Dworski S, Allison W and Ellis J 2004 *Phys. Rev. Lett.* **93** 156103

[3] Farías D and Rieder H K 1998 *Rep. Prog. Phys.* **61** 1575

[4] Graham A P 2003 *Surf. Sci. Rep.* **49** 115–168

[5] Groß A 2009 *Theoretical surface science* (Springer)

[6] Esbjerg N and Nørskov J K 1980 *Phys. Rev. Lett.* **45**(10) 807–810

[7] Rieder K H and García N 1982 *Phys. Rev. Lett.* **49** 43–46

[8] Petersen M, Wilke S, Ruggerone P, Kohler B and Scheffler M 1996 *Phys. Rev. Lett.* **76** 995

[9] Ellis J, Hermann K, Hofmann F and Toennies J P 1995 *Phys. Rev. Lett.* **75**(5) 886–889

[10] Montalenti F, Trioni M, Brivio G and Crampin S 1996 *Surf. Sci.* **364** L595–L599

[11] Martinez-Casado R, Usvyat D, Mallia G, Maschio L, Casassa S, Ellis J, Schültz M and Harrison N M 2014 *Phys. Chem. Chem. Phys.* **16**(39) 21106–21113

[12] Kohn W and Sham L J 1965 *Phys. Rev.* **140** A1133

[13] Jones R O and Gunnarsson O 1989 *Rev. Mod. Phys.* **61** 689

[14] Hedin L and Lundqvist B I 1971 *J. Phys. C: Solid State Phys.* **4** 2064

[15] von Barth U and Hedin L 1972 *J. Phys. C: Solid State Phys.* **5** 1629

[16] Gunnarsson O and Lundqvist B I 1976 *Phys. Rev. B* **13** 4274

[17] Langreth D C and Mehl M J 1981 *Phys. Rev. Lett.* **47** 446

[18] Perdew J P, Chevary J A, Vosko S H, Jackson K A, Pederson M R, Singh D J and Fiolhais C 1992 *Phys. Rev. B* **46** 6671

[19] Perdew J P, Burke K and Ernzerhof M 1996 *Phys. Rev. Lett.* **77** 3865

[20] Nardelli M B 1996 *Solid State Commun.* **97** 215–219

[21] Silva J L F D, Stampfl C and Scheffler M 2003 *Phys. Rev. Lett.* **90**(6) 066104

[22] Jean N, Trioni M I, Brivio G P and Bortolani V 2004 *Phys. Rev. Lett.* **92**(1) 013201

[23] Schüller A, Winter H, Gravielle M S, Pruneda J M and Miraglia J E 2009 *Phys. Rev. A* **80** 062903

[24] de Lara-Castells M P, Stoll H and Mitrushchenkov A O 2014 *J. Phys. Chem. A* **118** 6367–6384

[25] Grimme S 2006 *J. Comput. Chem.* **27** 1787–1799

[26] Grimme S, Antony J, Ehrlich S and Krieg H 2010 *J. Chem. Phys.* **132** 154104

[27] Ruiz V G, Liu W, Zojer E, Scheffler M and Tkatchenko A 2012 *Phys. Rev. Lett.* **108**(14) 146103

[28] Dion M, Rydberg H, Schröder E, Langreth D C and Lundqvist B I 2004 *Phys. Rev. Lett.* **92** 246401

[29] Klimeš J, Bowler D R and Michaelides A 2010 *J. Phys.: Condens. Matter* **22** 074203

[30] Lee K, Murray É D, Kong L, Lundqvist B I and Langreth D C 2010 *Phys. Rev. B* **82** 081101

[31] Klimeš J, Bowler D R and Michaelides A 2011 *Phys. Rev. B* **83** 195131

[32] Silvestrelli P L 2008 *Phys. Rev. Lett.* **100** 053002

[33] Silvestrelli P L, Ambrosetti A, Grubisiĉ S and Ancilotto F 2012 *Phys. Rev. B* **85** 165405

[34] Knowles P J, Hampel C and Werner H 1993 *J. Chem. Phys.* **99** 5219–5227 ISSN 0021-9606

[35] Grimme S, Ehrlich S and Goerigk L 2011 *J. Comput. Chem.* **32** 1456–1465

[36] del Cueto M, Muzas A S, Füchsel G, Gatti F, Martín F and Díaz C 2016 *Phys. Rev. B* **93** 060301

[37] del Cueto M, Maurer R J, Al Taleb A, Farías D, Martín F and Díaz C 2019 *J. Phys.: Condens. Matter* **31** 135901

[38] Minniti M, Díaz C, Cuñado J L F, Politano A, Maccariello D, Martín F, Farías D and Miranda R 2012 *J. Phys.: Condens. Matter* **24** 354002

[39] Maurer R J, Ruiz V G and Tkatchenko A 2015 *J. Chem. Phys.* **143** 102808 ISSN 0021-9606

[40] Meng G, Yin R, Zhou X and Jiang B 2021 *J. Phys. Chem. C* **125** 24958–24966

[41] Kresse G and Hafner J 1993 *Phys. Rev. B* **47** 558

[42] Kresse G and Hafner J 1994 *Phys. Rev. B* **49** 14251

[43] Kresse G and Furthmüller J 1996 *Comput. Mater. Sci.* **6** 15–50

[44] Kresse G and Furthmüller J 1996 *Phys. Rev. B* **54** 11169

[45] Blöchl P E 1994 *Phys. Rev. B* **50** 17953

[46] Kresse G and Joubert D 1999 *Phys. Rev. B* **59** 1758

[47] Methfessel M and Paxton A T 1989 *Phys. Rev. B* **40** 3616

[48] Laurent G, Martín F and Busnengo H F 2009 *Phys. Chem. Chem. Phys.* **11** 7303–7311

[49] Zhang Y and Yang W 1998 *Phys. Rev. Lett.* **80** 890

[50] Hammer B, Hansen L B and Nørskov J K 1999 *Phys. Rev. B* **59** 7413

[51] Perdew J P, Ruzsinszky A, Csonka G I, Vydrov O A, Scuseria G E, Constantin L A, Zhou X and Burke K 2008 *Phys. Rev. Lett.* **100** 136406

[52] Tkatchenko A and Scheffler M 2009 *Phys. Rev. Lett.* **102** 073005

[53] Berland K, Cooper V R, Lee K, Schröder E, Thonhauser T, Hyldgaard P and Lundqvist B I 2015 *Rep. Prog. Phys.* **78** 066501

[54] Hamada I 2014 *Phys. Rev. B* **89** 121103

[55] Sabatini R, Gorni T and de Gironcoli S 2013 *Phys. Rev. B* **87** 041108

[56] Peng H, Yang Z H, Perdew J P and Sun J 2016 *Phys. Rev. X* **6** 041005

[57] Chakraborty D, Berland K and Thonhauser T 2020 *J. Chem. Theory Comput.* **16** 5893–5911

[58] Busnengo H F, Salin A and Dong W 2000 *J. Chem. Phys.* **112** 7641–7651

[59] Gravielle M S, Bocán G A and Díez Muiño R 2010 *Phys. Rev. A* **82**(5) 052904

[60] Rubiano C A R, Bocan G A, Gravielle M S, Bundaleski N, Khemliche H and Roncin P 2013 *Phys. Rev. A* **87**(1) 012903

[61] Muzas A, Martín F and Díaz C 2015 *Nucl. Instrum. Methods Phys. Res. B* **354** 9–15 ISSN 0168-583X 26th International Conference on Atomic Collisions in Solids

[62] Bocan G A, Fuhr J D and Gravielle M S 2016 *Phys. Rev. A* **94**(2) 022711

[63] del Cueto M, Muzas A, Martín F and Díaz C 2020 *Nucl. Instrum. Methods Phys. Res. B* **476** 1–9 ISSN 0168-583X

[64] Bocan G A, Breiss H, Szilasi S, Momeni A, Staicu Casagrande E M, Sánchez E A, Gravielle M S and Khemliche H 2021 *Phys. Rev. B* **104**(23) 235401

[65] Muzas A S, Frisco L, Bocan G A, Díaz C and Gravielle M S 2024 *Phys. Rev. A* **109**(4) 042823

[66] Stoer J and Burlisch R 1980 *Introduction to Numerical Analysis* (New York: Springer)

[67] Ray C J and Bowman J M 1975 *J. Chem. Phys.* **63** 5231–5234

[68] Ray C J and Bowman J M 1977 *J. Chem. Phys.* **66** 1122–1126

[69] Park S C and Bowman J M 1984 *Chem. Phys. Lett.* **110** 383–384

[70] Farías D, Díaz C, Riviére P, Busnengo H F, Nieto P, Somers M F, Kroes G J, Salin A and Martín F 2004 *Phys. Rev. Lett.* **93**(24) 246104

[71] Díaz C, Busnengo H F, Rivière P, Farías D, Nieto P, Somers M F, Kroes G J, Salin A and Martín F 2005 *J. Chem. Phys.* **122** 154706

[72] Díaz C, Somers M F, Kroes G J, Busnengo H F, Salin A and Martín F 2005 *Phys. Rev. B* **72**(3) 035401

[73] Díaz C, Rivière P and Martín F 2009 *Phys. Rev. Lett.* **103**(1) 013201

[74] Laurent G, Barredo D, Farías D, Miranda R, Díaz C, Rivière P, Somers M F and Martín F 2010 *Phys. Chem. Chem. Phys.* **12** 14501–14507

[75] Díaz C, Martín F, Kroes G J, Minniti M, Farías D and Miranda R 2012 *J. Phys. Chem. C* **116** 13671–13678

[76] Meyer H D, Vendrell O, Worth G A, Beck M H and Jäckle A 2013 The Heidelberg MCTDH Package, Versions 8.2–8.5. Available at http://mctdh.uni-hd.de

[77] Meyer H D and Worth G A 2003 *Theor. Chem. Acc.* **109** 251–267

[78] Beck M H, Jäckle A, Worth G A and Meyer H D 2000 *Phys. Rep.* **324**(1) 1–105

[79] Meyer H D, Gatti F and Worth G A 2009 *Multidimensional Quantum Dynamics: MCTDH Theory and Applications* (John Wiley & Sons)

[80] Meyer H D 2012 *WIREs Comput. Mol. Sci.* **2** 351–374

[81] van Harrevelt R and Manthe U 2004 *J. Chem. Phys.* **121**(8) 3829–3835

[82] Crespos C, Meyer H D, Mowrey R C and Kroes G J 2006 *J. Chem. Phys.* **124** 074706

[83] Krishnamohan G P, Olsen R A, Kroes G J, Gatti F and Woittequand S 2010 *J. Chem. Phys.* **133** 144308

[84] Muzas A S, Gatti F, Martín F and Díaz C 2016 *Nucl. Instrum. Meth. Phys. Res. B* **382** 49–53

[85] Nihill K J, Hund Z M, Muzas A S, Díaz C, del Cueto M, Frankcombe T, Plymale N T, Lewis N S, Martín F and Sibener S J 2016 *J. Chem. Phys.* **145**(8) 084705

[86] Füchsel G, Thomas P S, den Uyl J, Öztürk Y, Nattino F, Meyer H D and Kroes G J 2016 *Phys. Chem. Chem. Phys.* **18** 8174–8185

[87] Meng Q and Meyer H D 2015 *J. Chem. Phys.* **143** 164310

[88] Meng Q and Meyer H D 2017 *J. Chem. Phys.* **146**(18) 184305

[89] Meng Q, Schröder M and Meyer H D 2021 *J. Chem. Theory Comput.* **17**(5) 2702–2713

[90] del Cueto M, Zhou X, Muzas A S, Díaz C, Martín D, Jiang B and Guo H 2019 *J. Phys. Chem. C* **123**(26) 16223–16231

[91] del Cueto M, Muzas A S, Frankcombe T J, Martín F and Díaz C 2019 *Phys. Chem. Chem. Phys.* **21**(28) 15879–15887

[92] Jäckle A and Meyer H D 1996 *J. Chem. Phys.* **104** 7974–7984

[93] Jäckle A and Meyer H D 1998 *J. Chem. Phys.* **109** 3772–3779

[94] Schlichting H, Menzel D, Brunner T and Brenig W 1992 *J. Chem. Phys.* **97** 4453–4467

[95] Berenbak B, Zboray S, Riedmuller B, Papageorgopoulos D C, Stolte S and Kleyn A W 2002 *Phys. Chem. Chem. Phys.* **4** 68–74

[96] Hayes W W and Manson J R 2007 *Phys. Rev. B* **75** 113408

[97] Ueta H, Gleeson M A and Kleyn A W 2011 *J. Chem. Phys.* **134** 034706

[98] Rodríguez-Fernández A, Bonnet L, Crespos C, Larrégaray P and Díez Muiño R 2019 *J. Phys. Chem. Lett.* **10** 7629–7635

[99] Rodríguez-Fernández A, Bonnet L, Crespos C, Larrégaray P and Díez Muiño R 2020 *Phys. Chem. Chem. Phys.* **22**(39) 22805–22814

[100] Ren X, Rinke P and Scheffler M 2009 *Phys. Rev. B* **80** 045402

[101] Oudot B and Doblhoff-Dier K 2024 *J. Chem. Phys.* **161** 054708